nature nanotechnology

SUPPLEMENTARY INFORMATION

https://doi.org/10.1038/s41565-019-0609-5

In the format provided by the authors and unedited.

A highly reflective biogenic photonic material from core–shell birefringent nanoparticles

Benjamin A. Palmer[1,2,9*], Venkata Jayasurya Yallapragada[3,9], Nathan Schiffmann[1], Eyal Merary Wormser[4], Nadav Elad[5], Eliahu D. Aflalo[6,7], Amir Sagi[6,8], Steve Weiner[1], Lia Addadi[1] and Dan Oron[3*]

[1]Department of Structural Biology, Weizmann Institute of Science, Rehovot, Israel. [2]Present address: Department of Chemistry, Ben-Gurion University of the Negev, Beer-Sheva, Israel. [3]Department of Physics of Complex Systems, Weizmann Institute of Science, Rehovot, Israel. [4]Department of Chemical Engineering, Ben-Gurion University of the Negev, Beer-Sheva, Israel. [5]Department of Chemical Research Support, Weizmann Institute of Science, Rehovot, Israel. [6]Department of Life Sciences, Ben-Gurion University of the Negev, Beer-Sheva, Israel. [7]Department of Life Sciences, Achva Academic College, Arugot, Israel. [8]The National Institute for Biotechnology in the Negev, Ben-Gurion University of the Negev, Beer-Sheva, Israel. [9]These authors contributed equally: Benjamin A. Palmer, Venkata Jayasurya Yallapragada. **One sentence summary**: The birefringence of isoxanthopterin crystalline spherulites enhances the reflectivity of a biological photonic crystal. *e-mail: Bpalmer@bgu.ac.il; Dan.Oron@weizmann.ac.il

Supplementary Information

A Highly Reflective Biogenic Photonic Material from Core-Shell Birefringent Nanoparticles

Authors: Benjamin A. Palmer, Venkata Jayasurya Yallapragada, Nathan Schiffmann, Eyal Merary Wormser, Nadav Elad, Eliahu D. Aflalo, Amir Sagi, Steve Weiner, Lia Addadi, and Dan Oron

Figures S1-S5

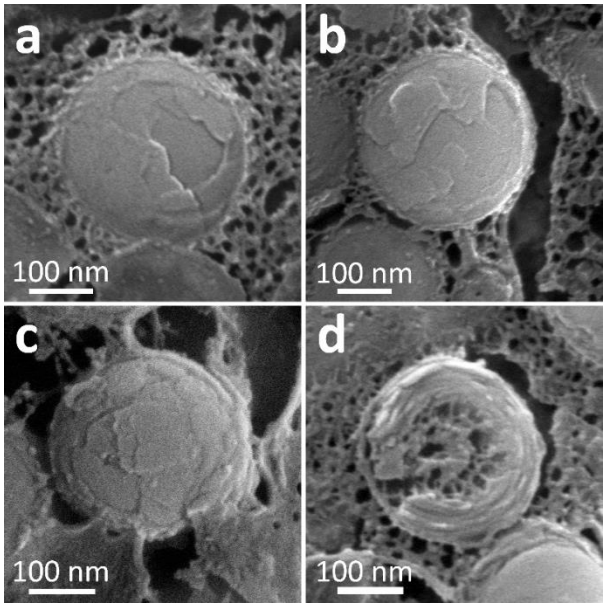

Supplementary Fig. S1. *In situ* imaging of isoxanthopterin nanoparticles. Cryo-SEM micrographs of whole (**a-c**) and fractured (**d**) isoxanthopterin nanoparticles from the tapetum reflector of *L. vannamei* obtained from longitudinal sections through the eye following high-pressure-freezing and freeze-fracture.

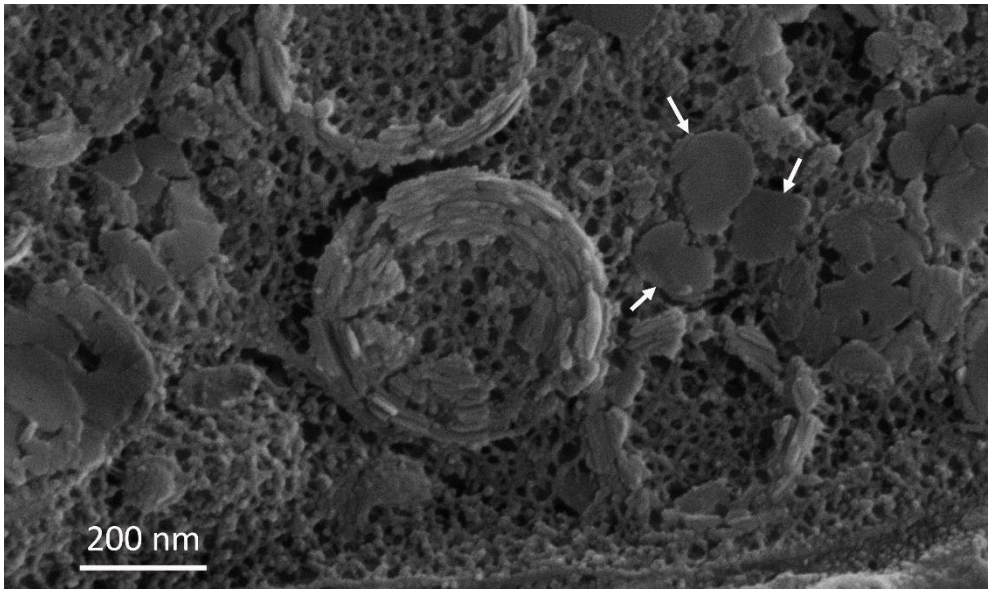

Supplementary Fig. S2. *In situ* imaging of isoxanthopterin nanoparticles. A cryo-SEM micrograph of fractured isoxanthopterin nanoparticles from the eye of *L. vannamei* following high-pressure-freezing and freeze-fracture. Individual isoxanthopterin platelets are observed in the vicinity of intact particles (marked by arrows).

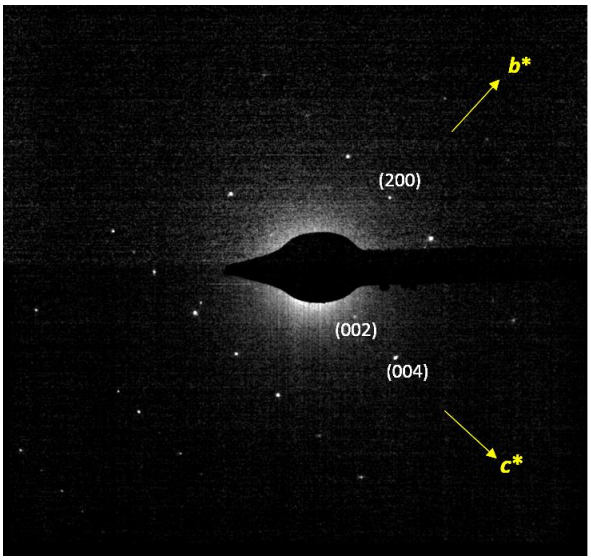

Supplementary Fig. S3. Electron diffraction of isoxanthopterin crystal platelets. Observed *0kl* electron diffraction pattern obtained by irradiating isoxanthopterin crystal plates perpendicular to the plate face (i.e., down the *a** axis). Along b* only even reflections are observed with a *d* spacing of 5.37 Å which is half the *b* axis of isoxanthopterin (*Cmca*, a = 6.2877 Å, b = 10.68 Å, c = 19.97 Å), consistent with the reflection condition for *Cmca* symmetry *0kl*: k = 2n. The *d* spacing measured along the *00l* line is 10.1 Å which is half the value of *c* axis, consistent with the *Cmca* reflection condition *00l: l* = 2n.

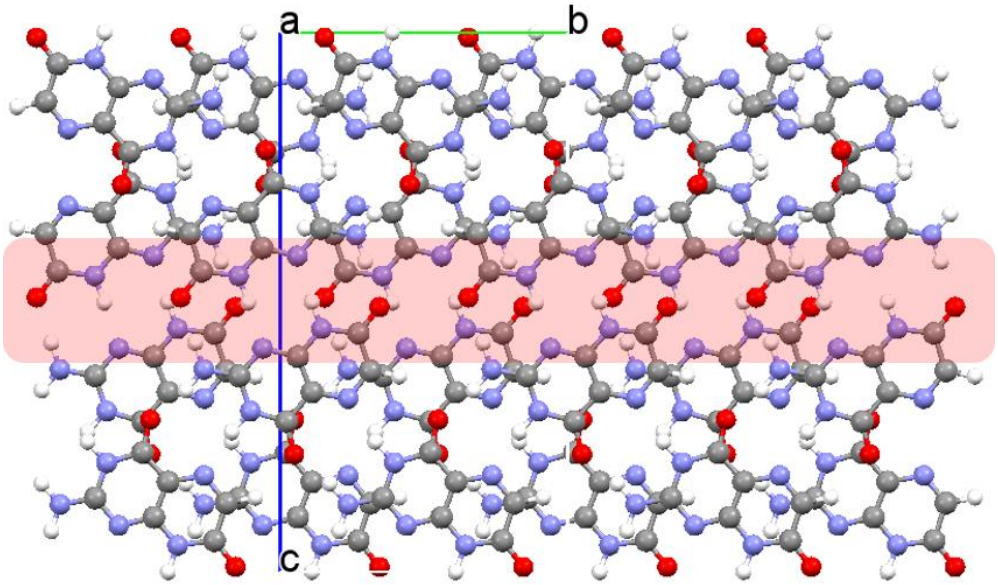

Supplementary Fig. S4. Explanation of observed lattice fringe periodicity in Figure 2. Lattice fringes with a periodicity of 10.2 Å are observed in images of 2D slices from TEM tomogram reconstructions at different heights through the lower shell of the nanoparticles (Fig. 2 g,h). We attribute this spacing to half of the *c*-axis of isoxanthopterin (*c* = 19.98 Å). Along the direction of the *c*-axis the crystal structure of isoxanthopterin contains electron dense layers of molecules, interrupted by less-dense regions half way along the unit cell (marked by transparent red band) corresponding to arrays of H-bonding between isoxanthopterin molecules.

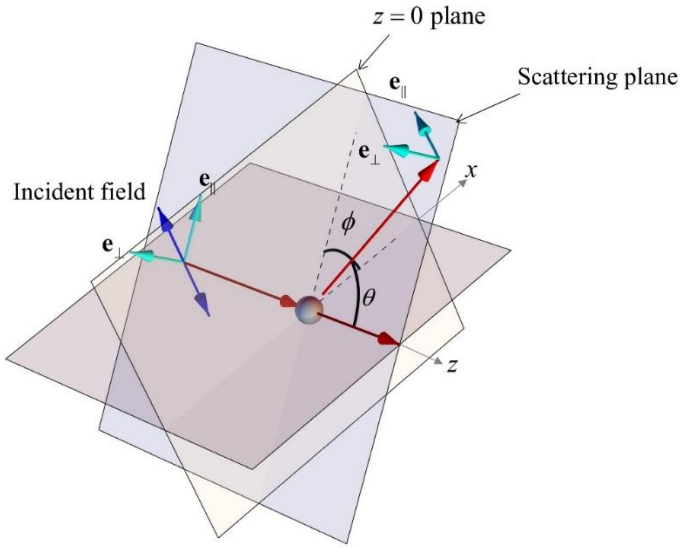

Supplementary Fig. S5. Scattering geometry. The scattering geometry employed in the discussion of Mie theory. The incident field and scattered field resolved into components parallel and perpendicular to the scattering plane. The scattered intensity measured at a point on the scattering plane is proportional to the modulus squared of the total field. The

incident field propagates along the positive *z* direction towards the nanosphere located at the origin.

Materials and Methods

Specimen Collection and Preparation. Adult specimens of *L. vannamei* were grown and maintained at the Ben-Gurion University of the Negev aqua facility under the following conditions: Water temperature was maintained at 27 ± 1 °C, photoperiod of 12 h light:12 h dark. Food comprised shrimp pellets (30% protein; Rangen) *ad libitum* three times a week. Water quality was assured by circulating the entire water volume through a biofilter maintaining all of the required water physicochemical parameters: pH 8.3 ± 0.5, nitrite <0.1 mg·L−1, nitrate <50 mg/L, ammonium levels were negligible, and oxygen levels were >5 mg·L−1. *L. vannamei* specimens were maintained under complete dark conditions for 24 h (dark-adaptation) before eyestalk collection. Animals were anesthetized in ice-cold water before dissection. The eyestalks were removed from the animal under red illumination to maintain the eyes in the dark-adapted state. The eyestalks were then fixed in 4% paraformaldehyde and 2.5% glutaraldehyde in 0.1 M cacodylate buffer, or alternatively in 4% paraformaldehyde in 1× PBS, in the dark. The eyestalks were fixed for 24 h before the cornea was removed manually using a scalpel. The eyestalks were then placed back into the fixative solution until they were used for further experimentation, usually within a period of 48–72 h from extraction. Eye sections were obtained by embedding the fixed eyestalks in 7% agar (using 1× PBS as the medium) and cut into 200-μm longitudinal and horizontal sections (respectively parallel and perpendicular to the eye axis), using a vibratome (OTS 400; EMS).

Light Microscopy. Light microscopy and polarized light microscopy imaging on fixed eye sections was performed using a Nikon Eclipse E600WPOL microscope equipped with a

Nikon Digital Sight DS-Fi1-U2 camera using reflection, transmission, or polarization mode with 2.5×, 5×, 10×, 20× and 50× air objectives.

Cryo-SEM imaging. The eye sections were cut to size, sandwiched between two metal discs (3 mm in diameter with 0.1 mm cavities), and cryo-immobilized in a 10% dextran solution as a cryo-protectant in a high-pressure freezing device (EM ICE; Leica). The frozen samples were mounted on a holder under liquid nitrogen and transferred to a freeze-fracture device (BAF60; Bal-Tec) using a vacuum cryotransfer device (VCT 100; Bal-Tec). Specimens were then taken to the cryo-SEM, etched for 5-10 min at -105 °C, and transferred back to the freeze-fracture device to be coated with 4 nm of Pt. Samples were then observed in an Ultra 55 SEM (Zeiss) using a secondary electron in-lens detector, maintaining the frozen-hydrated state with a cryo-stage operating at a temperature of −120 °C. Measurements of the diameter of the nanoparticles were performed from the cryo-SEM micrographs on the nanoparticles that appeared to be at the fracture surface, using ImageJ software.

TEM imaging, electron diffraction and TEM tomography. Longitudinal eye sections typically 300 μm thick (tapetum and proximal layers together or separated) were cut, immersed in double distilled water (DDW) in a small glass vial and gently agitated on a rocking plate overnight. Observations in the optical microscope demonstrated that the crystalline nanoparticles are readily liberated from the tissue after a few minutes of agitation. In order to disrupt the nanoparticles to their single platelet components, further sonication and ultra-sonication was applied to the tissue in solution, and the supernatant was isolated. A suspension of the crystals in DDW was then removed and a drop was applied to a glow-discharged homemade carbon-coated, copper TEM grid. The suspension

was allowed to settle for 45 seconds and blotted. Samples were observed with a Tecnai T12 transmission electron microscope operated at 120 kV. Images and diffraction patterns were recorded on a Gatan OneView camera using imaging and diffraction modes respectively. Measurements of the nanoparticle diameter and shell thickness were performed from the TEM micrographs using ImageJ. Tomographic tilt series were recorded with a Tecnai TF20 electron microscope. Experiments were performed at 200 kV, with extraction voltage 3850 V, gun lens 6, spot size 3, a condenser aperture of 50 μm and an objective aperture of 100 μm. Alignment was performed to maximize parallel illumination. Movies were recorded on a K2 Summit direct detector (Gatan) mounted at the end of a GIF Quantum energy filter (Gatan) using a slit of 20 eV. Movies were collected in counting mode at a nominal magnification of 125,000× corresponding to a physical pixel size of 1.7 Å. Dose rate was set to ~17 electrons/Å^2/sec, with 4 sec exposures divided over 8 movie frames. The dose rate on the camera below the specimen was ~5 electrons/Å^2/sec on average. Tilt series were collected at a range of ±65° with 1° increment using SerialEM software[1]. The tomographic tilt series were CTF corrected, aligned using fiducial-less alignment and reconstructed using simultaneous iterative reconstruction technique (SIRT) as implemented in the IMOD software suite[2]. Reconstructions were visualized using IMOD and Chimera[3].

***In situ* back-scattering measurements.** Back-scattering of light was measured in-situ directly from eye sections using a previously-developed custom built microscope[4]. A small area of the tapetum was illuminated with white light from a xenon lamp, and the resulting scattering was collected with a high numerical aperture objective. Spectra were obtained using a fiber coupled spectrometer (Shamrock SR303i; Andor) equipped with a iDus 420

CCD cooled camera. The spectra were divided by the source spectrum (measured with a silver mirror), to get a qualitative understanding of the variation of reflectivity with wavelength.

Calculation of normalized scattering cross sections. The scattering properties of a small particle can be expressed in terms of a scattering cross section, which is the fraction of the intensity of the incident plane wave that is scattered. For a spherically symmetric particle, these cross sections can be calculated using Mie theory, in which both the incident and scattered fields are expressed as a linear combination of spherical harmonics, and the scattered amplitudes are determined by matching field components at the boundaries of the sphere. The scattering geometry is illustrated in Figure S5.

The results of the Mie calculation are used to calculate the vector scattering amplitude X, defined as follows.

$$\mathbf{X} = S_2 \cos\phi \mathbf{e}_{\parallel s} + S_1 \sin\phi \mathbf{e}_{\perp s}$$

The quantities *S*1 and *S*2, which are the scattering matrix elements, are functions of the scattering angle, and represent the scattered amplitudes of field components perpendicular and parallel to the scattering plane, respectively. $\mathbf{e}_{\parallel s}$ and $\mathbf{e}_{\perp s}$ (also functions of the scattering angle) are unit vectors parallel and perpendicular to the scattering plane respectively. For the case of the rotationally symmetric isoxanthopterin nanospheres, *S*1 and *S*2 are calculated using the modified Mie approach of refs. 30-32 (main text). Using these values, the total scattering cross section is obtained by computing the following integral.

$$Q_{\text{total}} = \frac{1}{\pi r^2} \int_{\theta=0}^{\pi} \int_{\phi=0}^{2\pi} \frac{|\mathbf{X}|^2}{k^2} \sin\theta d\theta d\phi$$

The back scattering cross section referred to in the paper is obtained by appropriately changing the limits of integration over Θ, as shown below.

$$Q_{\text{back}} = \frac{1}{\pi r^2} \int_{\theta=\frac{\pi}{2}}^{\pi} \int_{\phi=0}^{2\pi} \frac{|\mathbf{X}|^2}{k^2} \sin\theta d\theta d\phi$$

Here the integration is carried out only over the backward half solid angle. The expressions shown above include normalization by dividing by the physical area of cross section of the scattering sphere, and the resulting cross sections are dimensionless.

Computation of reflectivity of nanosphere arrays. In all the calculation of reflection properties of 3D arrays of nanospheres described in this work, the Finite Difference Time Domain (FDTD) method is employed[5]. Computations have been performed using a commercial grade FDTD solver[6]. The reflectivities of Figure 6 have been obtained by constructing 10 layers of spheres arranged in an FCC lattice, with the plane wave source injecting light normal to an interface parallel to the 111 plane of the FCC lattice. Bloch boundary conditions have been used in the lateral directions, and the simulation time has been set to 50 ps. The background index of the simulation was set as 1.33 (water). A uniform spatial grid of size 15 nm has been used for shell thicknesses above 70 nm, and 10 nm for thicknesses below 70 nm. The radial orientation of the optic axis in the shell has been specified by suitably specifying a "LC rotation" grid attribute for each individual nanosphere in the simulation domain[7]. The reflectivities so obtained are a sum over all the diffracted orders. In order to aid visualization, in Figure 6c the spectra have been binned by averaging the reflectivity values in frequency bins of with ~3.1 THz, corresponding to several nm per bin in the wavelength axis.

References

1 Mastronarde, D. N. Automated electron microscope tomography using robust prediction of specimen movements. *J. Struct. Biol.* **152**, 36-51 (2005).

2 Kremer, J. R., Mastronarde, D. N. & McIntosh, J. R. Computer visualization of three-dimensional image data using IMOD. *J. Struct. Biol.* **116**, 71–76 (1996).

3 Pettersen, E. F. *et al.* UCSF Chimera - a visualization system for exploratory research and analysis. *J. Comput. Chem.* **25**, 1605–1612 (2004).
4 Gur, D., Leshem, B., Oron, D., Weiner, S. & Addadi, L. The structural basis for enhanced silver reflectance in Koi fish scale and skin. *J. Am. Chem. Soc.* **136**, 17236-17242, (2014).
5 Taflove, A. & Hagness, S. C. *Computational Electrodynamics. The Finite-Difference Time-Domain Method*. Third edn, (ARTECH HOUSE, 2005).
6 https://www.lumerical.com/products/fdtd-solutions/.
7 https://kb.lumerical.com/materials_anisotropic_lc_grid_attribute.html.